PNAS RESEARCH ARTICLE | STATISTICS
BIOPHYSICS AND COMPUTATIONAL BIOLOGY

Band pattern formation of erythrocytes in density gradients is due to competing aggregation and net buoyancy

Felix Maurer[a,1], Camila Romero[a], Nikolas Lerch[a], Thomas John[a], Lars Kaestner[a,b], Christian Wagner[a,c], and Alexis Darras[a,d,1]

Affiliations are included on p. 7.

Edited by Anna Balazs, University of Pittsburgh, Pittsburgh, PA; received June 17, 2025; accepted November 3, 2025

Centrifugation of biological matter in density gradient solutions is a standard method for separating cell types or components. It is also used to separate red blood cells (RBCs) by age, as they lose water and become denser over their lifespan. When the density gradient is prepared with Percoll, discrete bands of RBCs are systematically observed along the gradient, despite the continuous density distribution of RBCs. Early studies suggested that cell aggregation might influence spatial distribution, but it remains debated whether a continuous density population can form discrete bands. We developed a continuity equation incorporating cell aggregation to describe the macroscopic evolution of RBC volume fraction in a density gradient, considering a continuous RBC density distribution. Numerical solutions demonstrate that the competition between net buoyancy and aggregation is sufficient to create band patterns. Our model reproduces the temporal evolution observed in experiments, but also predicts several types of bifurcation-like behaviors for the steady-state patterns in constant gradients, depending on RBC volume fraction and aggregation energy. This demonstrates that the competition between RBC aggregation and net buoyancy is a mechanism driving pattern formation.

pattern formation | density separation | cell aggregation | erythrocytes | DDFT

Significance

Density-based centrifugation is widely used to separate biological components, including red blood cells (RBCs) of different ages. However, puzzling banding patterns often appear in continuous gradients, and their origin has remained unclear. Here, we show that these patterns result from the interplay between cell aggregation and buoyant forces, with each band containing a mixture of cell ages. We developed a quantitative model that reproduces the observed patterns, enabling the design of customized gradients and cell concentrations to control or prevent band formation. For experimental implementation, we use syringe pumps to generate the gradients. This approach can optimize RBC age separation protocols and enhance the diagnostic use of band patterns in diseases affecting red blood cells.

Research into density gradient media started in the 1960s and led to advances in the separation protocols of biological matter by mass density (1–12). Density gradients are usually prepared by concentration gradients in suspensions of nanoparticles or macromolecular solutions, with sedimentation dynamics different from that of biological objects to separate (1–5). Among these media, suspensions of biocompatibly coated silica nanoparticles, known commercially as Percoll®, have found extensive utility in the separation of red blood cells (RBC) (5–12). Human RBCs remain approximately 120 d in the blood circulation. During their lifetime, they experience progressive dehydration, and the mass density consequently increases (13). Therefore, separation by density is considered a convenient way to sort RBCs according to their age (6, 7, 9). Previous studies reported characteristic discontinuous RBC distributions of distinct bands, referred to as heterogeneous fractionation (5–12), which we reproduce in Fig. 1 *B* and *H*. The underlying mechanism was unknown, sometimes attributed to intrinsic cell characteristics, e.g., heterogeneous ion exchange or cytoskeleton configurations (11). However, early observations of RBC redistribution after a second centrifugation indicated the presence of aggregation (6). Indeed, it is well known that, in polymer or nanoparticle suspensions, RBCs tend to aggregate into linear structures, called rouleaux, due to bridging and/or depletion forces (14–18). Therefore, the overall aggregation energy depends on both the properties of the RBCs, as well as on the properties of the suspension (19–22). We previously identified cell aggregation as an underlying mechanism significantly influencing band pattern formation thanks to a series of experiments where the aggregability of RBCs was altered (23). Now, we provide a numerical model that quantitatively predicts band pattern formation due solely to cell–cell aggregation, even if the mass density distribution is continuous.

Independently of the RBC density separation methods, the mechanics of pattern formation is a whole field of study on its own. Regular patterns, which are the result of a symmetry break, can appear in general dynamic instabilities, where two antagonistic processes compete for the dynamics of the system (e.g., Rayleigh–Bénard, Rayleigh–Taylor, and Benjamin–Feir instabilities) (24–26). Pattern formation is also closely related to biological systems, as it determines the morphogenesis of organisms (27–32). Paradigmatic models for microscopic systems include Turing patterns (from reaction–diffusion) and diffusion-aggregation mechanisms (33–38). Recently, it has also been

Author contributions: F.M., T.J., L.K., C.W., and A.D. designed research; F.M., C.R., and N.L. performed research; F.M. contributed new reagents/analytic tools; F.M. and C.R. analyzed data; and F.M. and A.D. wrote the paper.

The authors declare no competing interest.

This article is a PNAS Direct Submission.

[1]To whom correspondence may be addressed. Email: mail@felixmilanmaurer.com or alexis.darras@bristol.ac.uk.

This article contains supporting information online at https://www.pnas.org/lookup/suppl/doi:10.1073/pnas.2515704122/-/DCSupplemental.

Published December 19, 2025.

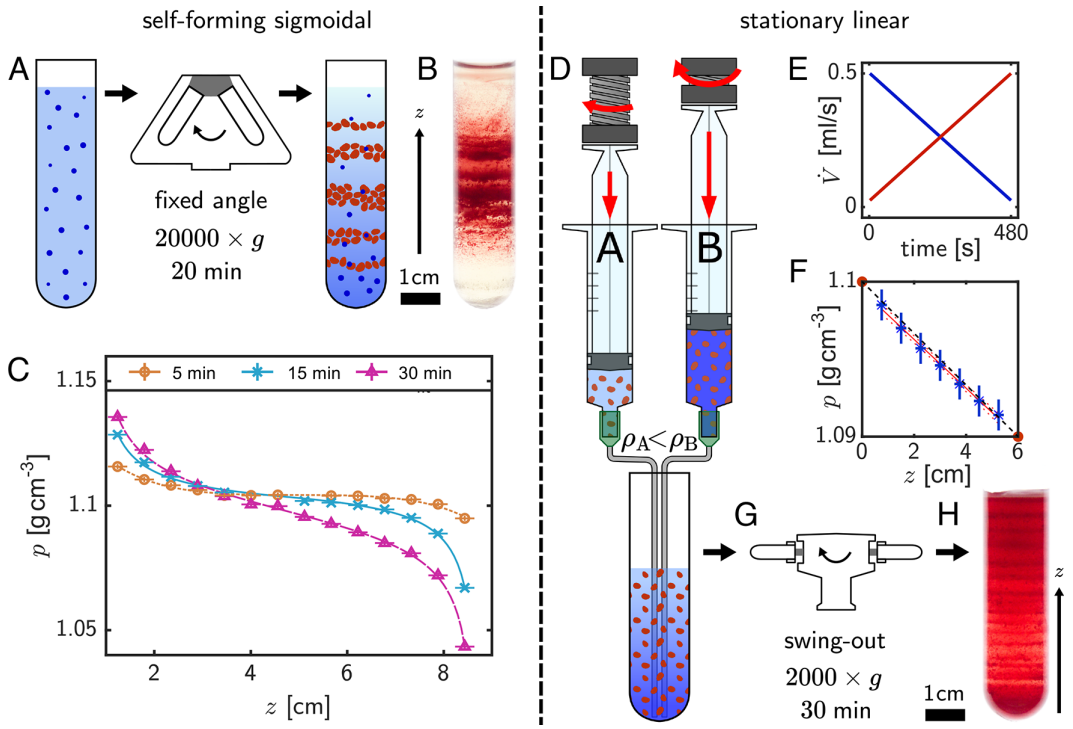

Fig. 1. Density gradient protocols for RBCs and resulting band patterns. (*Left* side) Self-forming gradient: (*A*) Scheme of a standard separation protocol. Packed RBCs are suspended in a Percoll medium matching the average cell density, with a hematocrit $\langle\psi\rangle$ of 2 %. The tube is placed in a fixed-angle rotor. Percoll particles form a concentration gradient and RBCs arrange in bands. (*B*) Photograph of the resulting experimental RBC distribution. The *z*-axis coincides with the tube axis. (*C*) Measurements of density from a self-formed gradient for different centrifugation durations T_c. Colored markers are measurements, while curves are regressions of a sigmoidal function (*SI Appendix*, Eq. **S2**). (*Right* side) Stationary linear gradient (*D*) Syringe pump setup: Syringes A and B hold Percoll-based media of different densities $\rho_A < \rho_B$ and equal hematocrit $\langle\psi\rangle$. The densities are chosen symmetrically around the mean cell density. Pistons are driven by linear actuators at different speeds during 8 min in 200 steps. (*E*) The flow rate is changed linearly and reversely between *A* and *B*. (*F*) Measurements of density from a resulting linear gradient. Marker lines show error bars, red dots mark the initial densities. A linear regression (red line) is close to the expected gradient (dashed line). (*G*) The gradient is centrifuged in a swing-out rotor. (*H*) Photograph of the resulting experimental RBC distribution in the tube, displaying a band pattern, for $\langle\psi\rangle = 4\,\%$.

shown that dynamic density functional theory (DDFT) can predict pattern formation with repulsive interactions, or "social distancing," when modeling disease transmission in a population (39). Among the possible patterns obtained in all these situations, band patterns are usually considered as the simplest ones, which can even appear in one-dimensional systems. However, their appearance and properties depend on the exact mechanisms and boundary conditions (e.g. as implemented in simulations, or determined by the experimental container size and shape) of the system in which they occur.

In this work, we present a continuum (DDFT) model that describes the macroscopic evolution of the distribution of RBCs in a Percoll gradient. It demonstrates that band patterns spontaneously form because of competition between isodensity equilibrium, i.e., net buoyant forces, and intercellular aggregation forces. Therefore, we identified the physical mechanisms leading to pattern formation in density gradients, which can reach clinical applications (12).

Protocols in biological or biochemical studies for age separation use spontaneous self-formation of a density gradient in Percoll, as sketched in Fig. 1 *A* and *B*. The RBCs suspended in the Percoll concentration gradient drift toward their isodensity position, where net buoyant force and external acceleration balance. This should result in a sorting by density. The spatial cell distribution is expected to represent the mass density distribution. However, when resolved in a Percoll gradient, the spatial distribution of RBCs organizes into a pattern of discrete and separate bands (5–12, 40); see Fig. 1 *B* and *H*. There is no indication that the mass density distribution of RBCs is discrete and/or multimodal. In fact, usually the distribution of the physiological RBC mass density is approximated as a Gaussian with a mean around $1.1\,\mathrm{g\,cm^{-3}}$ and a SD of $0.004\,\mathrm{g\,cm^{-3}}$ (41, 42).

We developed a numerical model under the assumption that RBCs interacting with a gradient of nanoparticles perceive the nanoparticles as a bulk medium. Consequently, the nanoparticles are not explicitly modeled. Instead, the gradient is represented by a density function $p(\mathbf{r}, t)$, which is introduced as an external field in the simulation. The dynamics of the RBCs are assumed to be governed by the acceleration of the net buoyant mass and cell aggregation. From a microscopic point of view, we consider the volume forces arising from the external acceleration due to centrifugation and the buoyancy following the principle of Archimedes, as well as the interaction forces between cells (Fig. 2).

The net buoyancy force combines the first two contributions. Acting on a single cell of volume V and mass density ρ at position $\mathbf{r}$, in a surrounding liquid of density $p(\mathbf{r}, t)$, it is given by $\mathbf{f}_{\mathrm{net}} = \mathbf{a}V(\rho - p(\mathbf{r}, t))$. We assume a constant inertial acceleration $\mathbf{a}$ due to the centrifugation of the sample, omitting the change over the tube length. RBCs are known to form rouleaux stacks, in which discocytes orient face-to-face, aligning their broad surfaces to maximize contact area. These linear chains can further interconnect, giving rise to extended networks. For the description of cell aggregation, we reduce the problem to pairwise interactions. Specifically, we introduce a *mean-field*

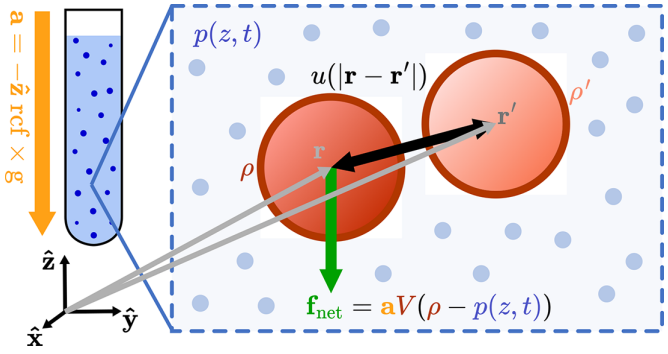

Fig. 2. Scheme of the microscopic mechanisms involved in the numerical model. RBCs are represented as spheres (red) with equal radii $r = 2.8\,\mu\mathrm{m}$ and different densities ρ and ρ' (red shading) suspended in a liquid medium of density $p(z,t)$ inside of a centrifugation tube in an acceleration field. The medium contains nanoparticles (blue, $r \approx 20\,\mathrm{nm}$ for Percoll, scaled up). Competing mechanisms acting on a cell are the net buoyant force $\mathbf{f}_{\mathrm{net}}$ and the interaction energy $u(|\mathbf{r}' - \mathbf{r}|)$ between cells with position vectors $\mathbf{r}$ and $\mathbf{r}'$.

potential. In the case of rouleaux, this potential is expected to be represented only by pair interaction. The principal mechanism is assumed to be as follows: a single probe cell finds a partner cell that is either at the boundary of an aggregate, e.g., at the end of a rouleaux stack, or unbound. In general, the interaction force between two cells depends on the initial relative orientation. However, our average potential is assumed to combine the average geometrical alignment path and forces. The interaction force is, therefore, assumed to originate from a spherically symmetric potential $\mathbf{f}_{\mathrm{int}} = \frac{\mathbf{r}-\mathbf{r}'}{|\mathbf{r}-\mathbf{r}'|}\nabla u(|\mathbf{r}-\mathbf{r}'|)$. The fundamental difference between equilibrium with and without cell aggregation becomes clear: without aggregation, a cell is at mechanical equilibrium if

$$\begin{aligned} 0 = \mathbf{f}_{\mathrm{net}} &= \mathbf{a}V(\rho - p(\mathbf{r},t)) \\ \Rightarrow \rho &= p(\mathbf{r},t), \end{aligned}$$

implying that the individual cell will find a position of matching mass density in the gradient. Equilibrium in the case of a pair aggregate requires

$$0 = \mathbf{f}_{\mathrm{net}} + \mathbf{f}_{\mathrm{int}} = \mathbf{a}V(\rho - p(\mathbf{r},t)) + \frac{\mathbf{r}-\mathbf{r}'}{|\mathbf{r}-\mathbf{r}'|}\nabla u(|\mathbf{r}-\mathbf{r}'|),$$

and is therefore determined by a competition between net buoyancy and interaction forces. In the case of a pair, the equilibrium solution is straightforward. The mean density is equal to the mean gradient density,

$$\rho + \rho' = p(\mathbf{r},t) + p(\mathbf{r}',t),$$

and the differences in buoyancy must be equalized by the interaction force

$$\mathbf{f}_{\mathrm{int}} = \frac{\mathbf{a}V}{2}\left(\rho - \rho' + p(\mathbf{r},t) - p(\mathbf{r}',t)\right).$$

Although governed by the same principle, the equilibrium configuration of multiple cells is considerably more complex. Within the framework of many-body computational systems, the feasible number of cells that can be modeled is sharply limited by computational constraints (23). This motivated the development of a bulk continuum description. Assuming that the dynamics take place in the Stokes regime, we compute cell flux terms originating from the microscopic forces. Due to the conservation of the number of RBCs, it is assumed that the volumetric cell density function $n(\mathbf{r},\rho,t)$, which describes the number of cells per volume element and mass density increment at position $\mathbf{r}$ and time t, satisfies a continuity equation

$$\partial_t n(\mathbf{r},\rho,t) = -\nabla_{\mathbf{r}} \cdot \mathbf{j}(\mathbf{r},\rho,t),\ \mathbf{j} = \mathbf{j}_{\mathrm{net}} + \mathbf{j}_{\mathrm{int}}. \qquad [1]$$

The flux $\mathbf{j}$ associated with a force $\mathbf{f}$ is given by the product of the volumetric cell density and a characteristic cell velocity $\mathbf{j} = n\mathbf{v}$. The velocity is obtained through the ratio between the force and the cell drag coefficient ζ, as $\mathbf{v} = \mathbf{f}\zeta^{-1}$. Therefore the flux associated with net buoyancy reads

$$\mathbf{j}_{\mathrm{net}}(\mathbf{r},\rho,t) = \zeta^{-1} n(\mathbf{r},\rho,t)\,\mathbf{a}V\,(\rho - p(z,t))\,.$$

The pair-interaction between cells leads to a flux

$$\mathbf{j}_{\mathrm{int}}(\mathbf{r},\rho,t) = \zeta^{-1}\iint n^{(2)}(\mathbf{r},\mathbf{r}',\rho,\rho',t)\nabla_{\mathbf{r}} u(|\mathbf{r}'-\mathbf{r}|)\,\mathrm{d}^3 r'\,\mathrm{d}\rho',$$

where $u(|\mathbf{r}' - \mathbf{r}|)$ is the pair interaction potential between RBCs and $n^{(2)}(\mathbf{r},\mathbf{r}',\rho,\rho',t)$ is the two-particle density function. The latter contains structural information of the geometrical configuration of cells in the equilibrium of the system. The quantity $n^{(2)}(\mathbf{r},\mathbf{r}',\rho,\rho',t)\,\mathrm{d}^3 r'\,\mathrm{d}\rho'$ represents the amount of cell matter at position $(\mathbf{r}',\rho')$ that interacts with the cell matter located at $(\mathbf{r},\rho)$. We use the approximation $n^{(2)}(\mathbf{r},\mathbf{r}',\rho,\rho',t) \approx g(|\mathbf{r}'-\mathbf{r}|)n(\mathbf{r},\rho,t)n(\mathbf{r}',\rho',t)$, where $g(r)$ is the *pair distribution function* (43, 44). This approximation is also known as the pair-factorization closure for a weakly inhomogeneous system within the local-equilibrium approximation. The pair distribution function $g(r)$ is assumed to be spherically symmetric, corresponding to an orientational average. In this mean-field approximation, the potential has spherical symmetry, even if the microscopic pair interaction is anisotropic (45). For systems of short linear chains, $g(r)$ exhibits a pronounced and narrow nearest-neighbor peak at the bond length, reflecting the strong localization of bonded pairs.

This peak is typically sharper and reaches higher amplitudes than in isotropic fluids, where nearest neighbors are distributed over a three-dimensional coordination shell, leading to a broader first peak. We assume that the RBC concentration remains homogeneous in the plane orthogonal to the tube axis. This implies a reduction to z dependency, $n(\mathbf{r},\rho,t) = n(z,\rho,t)$, which simplifies the continuity equation to one spatial dimension. Eventually, using a proper change of variables, the continuity equation [1] for the volume fraction of RBCs $\varphi = n(r,t)\,V^{-1}$, with RBC volume V, can then be written as

$$\begin{aligned} \zeta\partial_t\varphi = \frac{2\pi}{V}\partial_z\left(\varphi\int(z'-z)\,\tilde{u}(|z'-z|)\psi(z')\,\mathrm{d}z'\right) \\ + aV\partial_z\left(\varphi\,(\rho - p(z,t))\right), \end{aligned} \qquad [2]$$

where $\psi = \int\varphi\,\mathrm{d}\rho$, $\zeta = 8.97\times10^{-8}\,\mathrm{kg\,s^{-1}}$ is the Stokes drag coefficient of an RBC with hydrodynamic radius $R = 2.8\,\mu\mathrm{m}$ (46), $\tilde{u}(|\mathbf{r}-\mathbf{r}'|) = \int \mathrm{d}r' g(|\mathbf{r}-\mathbf{r}'|)\,u'(|\mathbf{r}-\mathbf{r}'|)$ is the effective interaction potential between two RBCs located at $\mathbf{r}$ and $\mathbf{r}'$, with $u'(r) = \partial_r u(r)$, $\mathbf{a} = -a\hat{\mathbf{z}}$ as the inertial acceleration in the centrifuge referential, and $p(z,t)$ the density of the surrounding Percoll suspension (47, 48). By this definition, $\psi(\mathbf{r},t)$ is the volume fraction of RBCs at location $\mathbf{r}$. The equilibrium of the system is given by $\partial_t\varphi = 0$, implying

$$\begin{aligned} \varphi\left(\int(z'-z)\,\tilde{u}(|z'-z|)\psi(z')\,\mathrm{d}z' + \frac{aV^2}{2\pi}\varphi\,(\rho - p(z,\infty))\right) \\ = 0, \end{aligned}$$

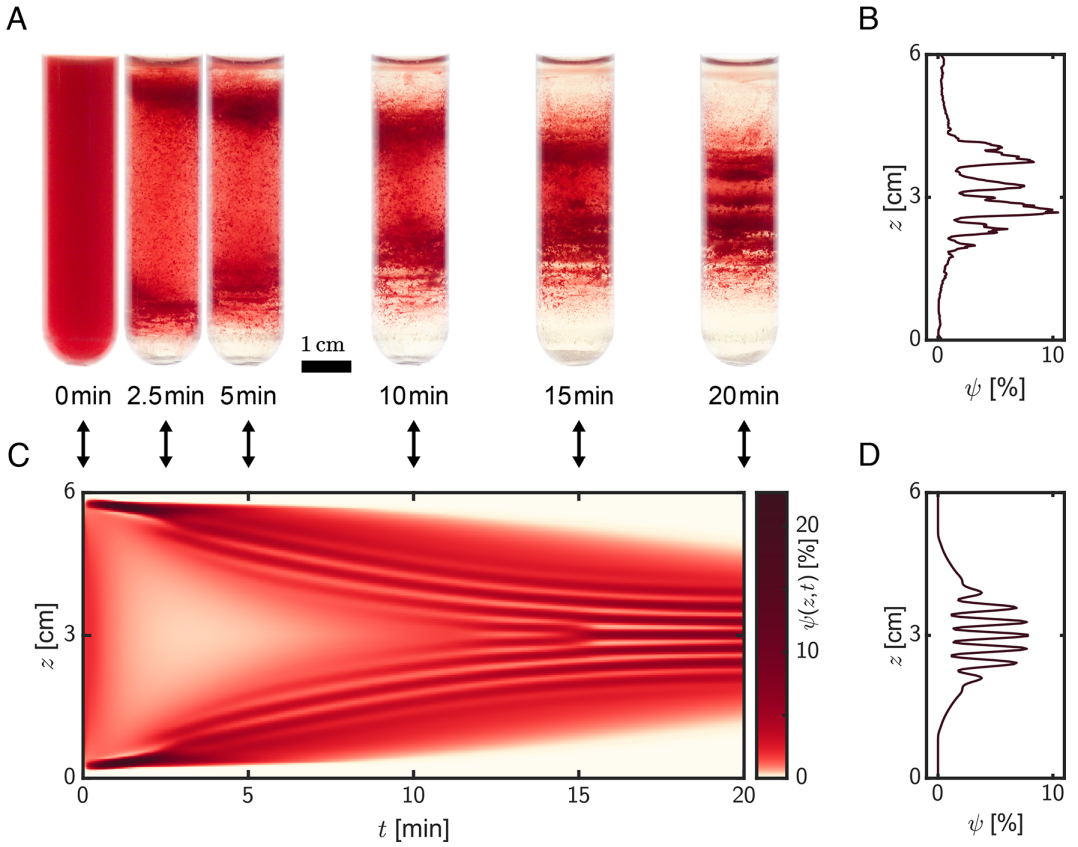

Fig. 3. RBC fractionation in a self-forming gradient: experiment and numerical solution. (*A*) Photographs from the separation protocol shown in Fig. 1 after different centrifugation durations T_c. The tube hematocrit was 2 %. Initially, the RBC sample was suspended homogeneously. The centrifugation was stopped after each time interval and an image was taken. During the first half of centrifugation, the enveloping RBC distribution shows two peaks that finally merged as a central band appeared at $t \gtrsim 15$ min. (*B*) Final experimental RBC density distribution ($t = 20$ min) showing distinct bands and a developed central band. The volume fraction $\psi(z)$ was obtained from image intensity profile measurements after a calibration under equal lighting conditions (see details in *SI Appendix*, section 5 and Fig. S5). (*C*) Numerical solution of the system with $\langle\psi\rangle = 2\,\%$ for comparison. The assumed gradient shape and gradient time development was designed to match measurements; see Fig. 1. The colormap was obtained from the calibration to photographs. Simulation results also show the separation in two peaks and a merging around $t \approx 15$ min with a central band. (*D*) Final numerical RBC density distribution ($t = 20$ min), showing distinct bands similar to the experiment.

which in the nontrivial case, $\varphi \neq 0$, portrays the competition between isodensity position and cell aggregation in the bulk. The solution without interaction is $\varphi(z, \rho, \infty) = \langle\psi\rangle L\, d_\rho(\rho)\delta(z - p^{-1}(\rho, \infty))$, where $d_\rho(\rho)$ is the physiological density distribution of RBCs, $\langle\psi\rangle$ the tube hematocrit, and L the tube length. The solution with interactions is contingent upon the particular form of the interaction under consideration. A common choice in the case of short-range interactions, like depletion, is a Lennard-Jones potential (49, 50),

$$u(r) = 4U\left(\frac{\sigma^{12}}{r^{12}} - \frac{\sigma^6}{r^6}\right).$$

The employed effective potential also takes into account the geometrical pair distribution function $g(r)$, i.e., $\tilde{u}(r) = \int g(r')\,\partial_r u(r')\,\mathrm{d}r'$. The effective potential employed in our numerical resolutions, along with further theoretical considerations, are provided in *SI Appendix* section 1. The numerical solver was implemented in C++ with CUDA; see *SI Appendix*, sections 3 and 4 and Figs. S3 and S4, and open-access code (51). We use $\sigma = 5.6\,\mu$m as the interaction range, i.e. the diameter of a sphere with the volume of human RBCs, which is around 90 fL (52).

To estimate the maximum possible band size without breakup, we need to analyze the scaling behavior and relative magnitudes of the competing terms. We begin by introducing a dimensionless system equation, examining the characteristic scaling of the relevant parameters,

$$\bar{u} = \frac{\tilde{u}}{U},\ \bar{z} = \frac{z}{\sigma},\ \bar{\rho} = \frac{\rho}{\sigma_\rho},\ \bar{p} = \frac{p}{\sigma_\rho},\ \bar{\varphi} = \varphi\sigma_\rho,\ \bar{t} = \frac{t}{\tau}.$$

The dimensionless potential is obtained through normalization by the amplitude U. The relevant length scale is the interaction length σ. In the case of a matched density gradient, the average density of the gradient is equal to the average density of the cell population $\langle\rho\rangle$, and the spread is chosen to match the width of the mass density distribution σ_ρ. We therefore normalize the mass density ρ, the gradient p, and the RBC concentration φ by the same characteristic density σ_ρ. Using $V \approx \frac{\pi}{6}\sigma^3$, the dimensionless system equation reads

$$\frac{\sigma\zeta}{aV\sigma_\rho\tau}\partial_{\bar{t}}\bar{\varphi} = \xi\,\partial_{\bar{z}}\left(\bar{\varphi}\int(\bar{z}' - \bar{z})\,\bar{u}(|\bar{z}' - \bar{z}|)\psi(\bar{z}')\,\mathrm{d}\bar{z}'\right) + \partial_{\bar{z}}\left(\bar{\varphi}\,(\bar{\rho} - \bar{p}(\bar{z}, \bar{t}))\right),\ \xi = \frac{12U}{aV\sigma_\rho\sigma}. \quad [3]$$

From the left-hand side, the dimensionless coefficient indicates that the characteristic time for the evolution of the RBC

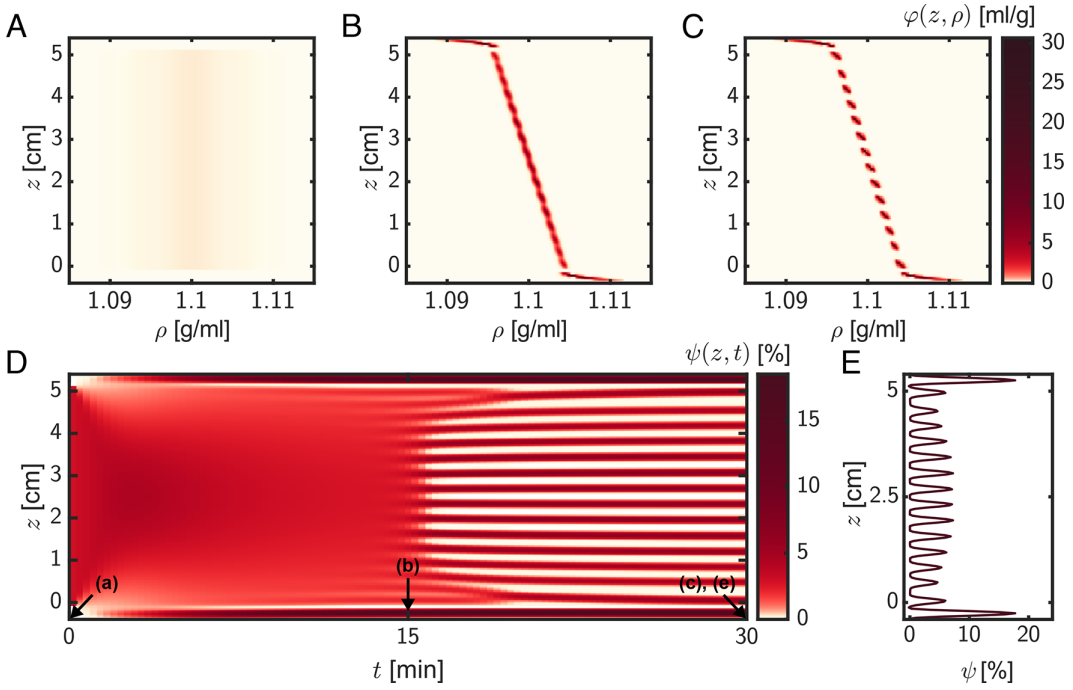

Fig. 4. Simulation results for sedimentation in a stationary linear gradient. The hematocrit was set to $\langle\psi\rangle = 3\,\%$. The prepared gradient from the protocol in Fig. 1**(d)** is modeled by $p(z) = 1.6\,\mathrm{g\,(ml\,cm)^{-1}}\,(z - 2.5\,\mathrm{cm}) + 1.1\,\mathrm{g\,ml^{-1}}$. **(a)-(c)** RBC density function $\varphi(z,\rho,t)$ at different time points during simulation (0, 15, and 20 min). Panel **(a)** shows the initial state of the RBC density function. It is homogeneous in space and follows the physiological density distribution assuming a Gaussian along the density dimension ρ. A time point near the onset of band formation is depicted in **(b)**. Panel **(c)** shows the final state, respectively, characterized by an overall alignment to the gradient but a superimposed band pattern. **(d)** Time evolution of the volume fraction $\psi(z,t)$. The distribution width is smallest at $t \approx 2$ min, when upward and downward moving cells are crossing in the middle of the sample tube. At $t \approx 15$ min distinct bands are forming which continue to sediment toward equilibrium. Also, a merging near the borders can be observed at $t \approx 17$ min. **(e)** The symmetric final state shows 14 bands, with accumulation localized in boundary tails generated by the density cut-off at the container walls.

concentration is $\tau = \sigma\zeta(aV\sigma_\rho)^{-1}$, reducing the scalings to a single parameter ξ. It is determined by the competition between the drag and the buoyant energy introduced by centrifugation. It also makes it clear that, if one considers an observation time much longer than the viscous transport time of the RBCs $\tau >> \frac{\sigma\zeta}{aV\sigma_\rho}$, a stationary solution will be observed, as the only term with an explicit dependence on $\partial_{\bar{t}}$ becomes negligible (as long as $\bar{p}(\bar{z},\bar{t})$ can be considered constant as a function of $\bar{t}$ during this characteristic time τ (i.e., $\partial_{\bar{t}}\bar{p} << 1$)). The prefactor ξ of the interaction integral compares the interaction energy $12U$ with the buoyant energy across the interaction length $aV\sigma_\rho\sigma$. This parameter ξ is negligible if the aggregation energy is very small compared to the characteristic buoyant energy $U << aV\sigma_\rho\sigma$, and the stationary distribution of RBCs is then expected to be very close to the solution without any interaction at all. Conversely, a significant deviation of the cell distribution from their isopycnic positions is to be expected for $U \gtrapprox aV\sigma_\rho\sigma$. The deviation of the cell density from the gradient corresponds to a spatial displacement Δz. If we assume a linear matched gradient $p = Gz$, dimensionless analysis leads to a characteristic difference $\bar{\rho} - \bar{p} = \Delta z\, G\sigma_\rho^{-1}$. We expect the interaction integral to scale with the average volume fraction $\langle\psi\rangle$. With that, the maximum displacement that can be stabilized by the interaction energy is $\Delta z \approx \sigma_\rho\xi\langle\psi\rangle G^{-1}$. For $U = 100\,\mathrm{aJ}$ in a system of length $L = 10^{-2}$ m with $\langle\psi\rangle = 10^{-2}$, and in a stationary linear gradient with $G \approx 2\sigma_\rho L^{-1}$, it is $\xi \approx 30$ and $\Delta z \approx 10^{-3}$ m. In addition to this estimation of the band distance, the competing terms in ξ also provide information about the influence of system parameters. While band distance decreases with increasing centrifugal acceleration a and gradient magnitude G, it increases with interaction energy U and mass density distribution width σ_ρ.

A more quantitative approach can be obtained with time resolutions of the system equation, with initial conditions considered as homogeneous in space, which corresponds to mixing the sample tube, and a physiological distribution in density $\varphi(z,\rho,0) = \langle\psi\rangle d_\rho(\rho) = \langle\psi\rangle(2\pi{\sigma_\rho}^2)^{-\frac{1}{2}} e^{-(\rho-\langle\rho\rangle)^2/2{\sigma_\rho}^2}$ with $\langle\rho\rangle = 1.1\,\mathrm{g\,cm^{-3}}$, $\sigma_\rho = 4\,\mathrm{mg\,cm^{-3}}$ (41, 42, 53). We solved the model for the traditional *self-forming sigmoidal* gradient, as well as a new *stationary linear* gradient separation protocol, in order to probe the properties of the obtained pattern in a simpler case. The interaction energy is fixed, and solutions for various spatially averaged volume fractions $\langle\psi\rangle$ are investigated.

The solution for the self-forming gradient protocol, illustrated in Fig. 1*A*, is depicted in Fig. 3. Experiments were performed with the mean Percoll density matching the mean RBC density (41, 42). Images after different centrifugation durations are shown in Fig. 3*A*. All figure data and raw images are available in a Figshare repository (54). Initially, the Percoll density is constant as the medium is homogeneous, $p(z, t = 0) = p_0$. Consequently, cells with a lower density than the surrounding medium, i.e., $\rho_{\mathrm{RBC}} < p_0$, initially move to the top and the remaining cells to the bottom. In the case of a perfect density match and a symmetrical mass density distribution, this divides the population exactly in half within the first minute. The dynamics then show two different time scales related to the two different sedimenting specimens, RBCs and Percoll particles. During the first minutes, RBCs reach their isopycnic position before the gradient fully develops. The isopycnic position with respect to each cell is therefore still changing over a longer

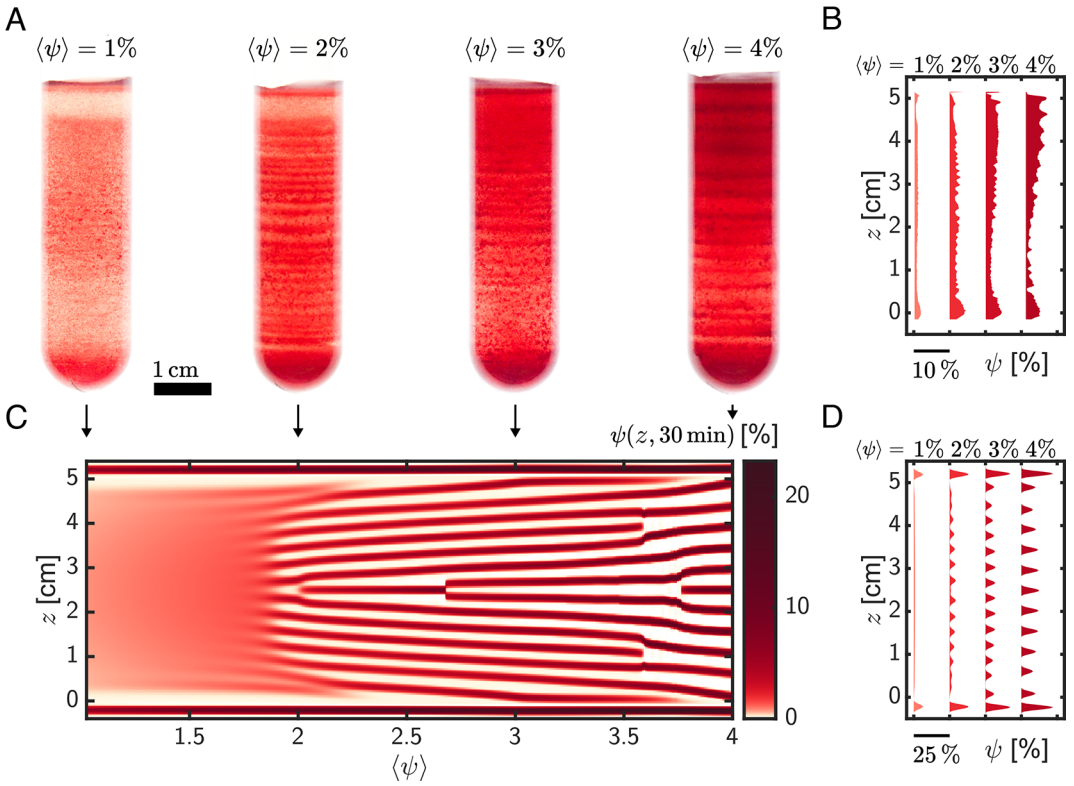

Fig. 5. Final band structures in linear gradients, for various hematocrits. (*A*) Experimental photographs for different hematocrits. Linear gradients were prepared following the protocol in Fig. 1*D*. The mean RBC density from one donor was measured and the density designed to cover range of 8 mg mL^{-1} symmetrically. All tubes were prepared and centrifuged at the same time. The meniscus level was 5 cm from the base of the tube. Accumulation at the boundaries arises from cells with densities outside the admissible range. (*B*) Extracted distribution of the volume fraction, based on the image intensity profiles. Bands appear starting at hematocrits above $\approx 1\,\%$. (*C*) Simulation end state for the same system size and different volume concentrations $\langle\psi\rangle$. There is a continuous emergence of a band pattern at hematocrits between 1 and 2 %. With increasing concentration, there are various bifurcations, including a change in final band positions and numbers. Abrupt transitions occur at around 2, 2.7 , 3.6, and 3.8 %. Overall, the distance between bands increases with hematocrit. (*D*) Distributions of the volume fraction in numerical simulations, for selected values of $\langle\psi\rangle$ matching the experimental hematocrits.

time scale until the end of centrifugation, meaning that the cell distribution follows the gradient formation dynamics. Hence, the gradient formation process also influences the pattern formation process. Microscopically, this observation can be explained by comparing the effective sedimentation coefficients of RBCs to those of Percoll particles in the system. The sedimentation coefficient of Svedberg in terms of the Stokes' law is proportional to the radius squared and the buoyant density difference (55). For RBCs, we arrive at $s_{\text{RBC}} \approx 1 \times 10^{-9}$ S to 1×10^{-10} S depending on the position in the gradient, and for silica particles at $s_{\text{silica}} \approx 1 \times 10^{-11}$ S. This implies that the time scale of RBC movement toward their buoyantly neutral position is 10 to 100 times smaller than the characteristic time of Percoll density gradient formation.

The numerically calculated RBC volumetric density $\psi(z, T_c)$ is in good agreement with the experimentally observed distribution, Fig. 3*C*. This includes time scales, i.e., the initial split $t < 2$ min, and the recombination with the development of a central band at around $t = 15$ min, as well as the number and relative amplitude of the bands. Differences include a breakup of the distribution tails in the top and bottom of the tube due to horizontal heterogeneity and uncontrollable variations in the experiment. Those variations might be induced by thermal or other convection, vibrations, and an offset in density matching.

An additional result for a higher hematocrit of 10 % in a self-forming gradient is shown in the *SI Appendix*, Fig. S7, revealing a lower number of bands with a higher population and increased spatial separation. At these higher hematocrit levels, the solutions are expected to be less reliable because local concentrations approach saturation ($\psi(z) = 100\,\%$), a regime in which the model assumptions are expected to break down. However, an overall agreement and confirmation of the scalings was observed.

We found that the model resolution leads to similar results when assuming a different shape of the effective potential $\tilde{u}$ as long as $\langle\tilde{u}\rangle = V^{-1}\int r^2\tilde{u}(r)\mathrm{d}r$ and the characteristic length σ remain approximately the same. The result for a different potential is shown and discussed in *SI Appendix*, section 6.

In order to perform concept-focused experiments, we designed controllable Percoll concentration gradients to study the final band pattern in various well-defined gradients and volume fractions. We use two computer-controlled syringe pumps to prepare a linear Percoll gradient and a homogeneous RBC distribution for the initial condition as shown in Fig. 1 *D*–*F*. This method uses lower accelerations, so that the distribution of Percoll does not change substantially during the sedimentation process. Hence, it can be realized with swing-out rotors. It is therefore more straightforward to implement corresponding numerical simulations, as the density gradient $p(z)$ can be considered stationary along time with $\partial_z p$ constant. Fig. 4 displays a typical time evolution obtained in the corresponding numerical simulation with a stationary linear density gradient. In this example, the distribution aligns with the gradient close to the expected equilibrium without interaction. This leads to an increase in the local volume fraction. The onset of the band pattern in this case appears afterward creating deviations from the equilibrium position without interaction.

Fig. 5 compares experimental and numerical outcomes. In a stationary linear gradient, a band pattern only appears above a critical concentration. Fig. 5*A* shows the final cell distribution after centrifugation under the same conditions for different hematocrits $\langle\psi\rangle$. It reveals a complex branching behavior in which the number of bands might increase or decrease with increasing hematocrit. Fig. 5*C* shows the simulation end state for different $\langle\psi\rangle$. The competition between net buoyant forces and aggregation can predict the emergence of various band patterns depending on the suspension properties and explains the high sensitivity of the band pattern on the experimental conditions. Indeed, for $\langle\psi\rangle > 3.5\,\%$, steady-state solutions exist only across a range of below $0.25\,\%$. In the experiment, the system is highly sensitive to perturbations, which can redistribute the RBCs through advection. Additionally, in 3D, we could also have heterogeneities appearing in the *xy*-plane, modifying the collision mechanisms toward a more stochastic process. Thus the observed bands are not cleanly separated, i.e., they are superimposed with a noise background. Also, a symmetry-breaking shift in the distribution can occur in case of a mismatch between the central gradient density and the average cell density; see Fig. 5*A* for $\langle\psi\rangle = 4\,\%$.

In this study, we proved that when aggregating particles with a nonunique mass density, such as RBCs, are placed in a density gradient, the assumption of an attractive pair interaction predicts band pattern formation in their spatial distribution. This occurs even if they have a monomodal and continuous mass density distribution. These findings are in agreement with the previous identification of cell aggregation as the most important mechanism in band pattern formation (23). Further, this aggregation seems unique to Percoll, as shown in the *SI Appendix*, section 8. Our continuum model provides an explanation for the time evolution during centrifugation and the final state of the RBC density function. This opens perspectives to model and predict properties of RBCs based on the observation of their band patterns, which has the potential of contributing to and enhance diagnostic predictions (12). Moreover, preparing controlled density gradients might allow to determine conditions to obtain more sensitive or more reproducible protocols to obtain pattern formations, which can now be explained theoretically. In summary, the competition between net buoyancy and aggregation is a physical mechanism generating pattern formation with a complex bifurcation diagram. Its comprehension presents an exciting challenge for researchers in the field of soft matter and biophysics, with potential clinical applications. Interestingly, although this pattern formation has now been observed with biological samples, we do not need to assume any specific biological properties to observe this effect, and it should occur with artificial particles of similar sizes and geometries.

Ethical Statement

Human blood withdrawal from healthy volunteers was performed after explicitly obtaining their informed consent. Blood withdrawal and handling were performed according to the Declaration of Helsinki. The ethics committee "Ärztekammer des Saarlandes" approved the full study protocol, permit number 176/21.

Materials and Methods

The preparation of physiological media of specific densities from Percoll involves adding 10xPBS for osmolarity adjustment, diluting with PBS for density adjustment, and adding HCl for pH adjustment (9, 23). Initially, a suspension of RBCs is mixed with a homogeneous Percoll medium in a centrifugation tube. The tube is then subjected to high accelerations $\geqslant 20{,}000 \times g$ for a duration of 20 min. Nano-sized Percoll particles then experience partial sedimentation and adopt a sigmoidal distribution. Control measurements of the density profiles without cells are shown in Fig. 1*C*. The density $p(z, t)$ of 14 layers extracted successively from the tube, 1 mL each, was measured using an Anton Paar Density Meter (DMA 4100M); see Fig. 1 *C* and *F*. To prepare a gradient of any desired shape, two syringe pumps are used. Syringe A holds a low-density medium with the desired hematocrit $\langle\psi\rangle$, and B a high-density medium, $\rho_B > \rho_A$, with the same cell concentration. The needle tips are joined in the tube bottom to achieve mixing (Fig. 1*D*). The volume flow is driven by linear actuators and varied to create a linear gradient (Fig. 1 *E* and *F*). Afterward the sample is placed in a swing-out centrifuge at $2{,}000 \times g$ for 30 min (Fig. 1*G*). An example of the resulting band pattern is depicted in Fig. 1*H*. Measurements were repeated for different durations of centrifugation T_c. The position z can empirically be linked to the Percoll density p via a sigmoidal function with time-dependent slope and curvature (2–4). The justification and properties of the chosen sigmoidal function used in the numerical model are detailed in the *SI Appendix*, section 2.

Data, Materials, and Software Availability. Band pattern formation of erythrocytes in density gradients is due to competing aggregation and net buoyancy (https://doi.org/10.6084/m9.figshare.29098733.v1) (54). The computational model is hosted on GitHub (https://github.com/FelixMaurer/RedPatterns) (51).

ACKNOWLEDGMENTS. A.D. acknowledges funding by the Young Investigator Grant of the Saarland University. C.W. acknowledges funding from the German Research Foundation by the research unit FOR 2688 Wa1336/12. We gratefully acknowledge the input of Chaouqi Misbah and Alexander Farutin of the Université Grenoble Alpes, as well as the computing time granted on the supercomputer MOGON II at JGU as part of NHR South-West.

Author affiliations: [a]Experimental Physics, Saarland University, Saarbrücken 66123, Saarland, Germany; [b]Theoretical Medicine and Biosciences, Saarland University, Homburg 66421, Saarland, Germany; [c]Physics and Materials Science Research Unit, University of Luxembourg, Esch-sur-Alzette L-4365, Luxembourg; and [d]School of Physics, University of Bristol, Bristol BS8 1TL, United Kingdom

1. G. M. Mateyko, M. J. Kopac, Part II: Isopyknotic cushioning during high-speed centrifugation. *Ann. N. Y. Acad. Sci.* **105**, 219–285 (1996).
2. H. Pertoft, T. C. Laurent, "Isopycnic separation of cells and cell organelles by centrifugation in modified colloidal silica gradients" in *Methods of Cell Separation*, N. Catsimpoolas, Ed. (Springer US, Boston, MA, 1977), pp. 25–65.
3. Tl. H. Pertoft, T. C. Laurent, L. Kagedal, Density gradients prepared from colloidal silica particles coated by polyvinylpyrrolidone (Percoll). *Anal. Biochem.* **88**, 271–282 (1978).
4. GE Healthcare, *Cell Separation Media, Methodology and Applications* (GE Healthcare, 2007).
5. L. Vettore, M. C. De Matteis, P. Zampini, A new density gradient system for the separation of human red blood cells. *Am. J. Hematol.* **8**, 291–297 (1980).
6. H. U. Lutz, P. Stammler, S. Fasler, M. Ingold, J. Fehr, Density separation of human red blood cells on self forming Percoll gradients: Correlation with cell age. *Biochim. Biophys. Acta (BBA): Gen. Subj.* **1116**, 1–10 (1992).
7. M. C. Wesseling *et al.*, Phosphatidylserine exposure in human red blood cells depending on cell age. *Cell. Physiol. Biochem.* **38**, 1376–1390 (2016).
8. A. Makhro, L. Kaestner, A. Bogdanova, "NMDA receptor activity in circulating red blood cells: Methods of detection" in *NMDA Receptors*, N. Burnashev, P. Szepetowski, Eds. (Springer New York, New York, NY, 2017), vol. 1677, pp. 265–282.
9. S. Kämpf *et al.*, Aging markers in equine red blood cells. *Front. Physiol.* **10**, 893 (2019).
10. R. Huisjes *et al.*, Density, heterogeneity and deformability of red cells as markers of clinical severity in hereditary spherocytosis. *Haematologica* **105**, 338–347 (2020).
11. A. Bogdanova, L. Kaestner, G. Simionato, A. Wickrema, A. Makhro, Heterogeneity of red blood cells: Causes and consequences. *Front. Physiol.* **11**, 392 (2020).
12. A Sadafi *et al.*, "Domain Adaptation and Representation Transfer, and Affordable Healthcare and AI for Resource Diverse Global Health" in *Sickle Cell Disease Severity Prediction from Percoll Gradient Images Using Graph Convolutional Networks*, S. Albarqouni *et al.*, Eds. (Springer, 2021), No. 1296812968, pp. 216–225.

13. P. Thiagarajan, C. J. Parker, J. T. Prchal, How do red blood cells die? *Front. Physiol.* **12**, 655393 (2021).
14. O. Baskurt, B. Neu, H. J. Meiselman, *Red Blood Cell Aggregation* (CRC Press, Boca Raton, FL, 2011), p. 2.
15. C. Wagner, P. Steffen, S. Svetina, Aggregation of red blood cells: From rouleaux to clot formation. *C. R. Phys.* **14**, 459–469 (2013).
16. O. Korculanin, T. Kochetkova, M. Lettinga, Competition between red blood cell aggregation and breakup: Depletion force due to filamentous viruses vs. shear flow. *Front. Phys.* **9**, 721368 (2021).
17. N. Moreno *et al*., Aggregation and disaggregation of red blood cells: Depletion versus bridging. *Biophys. J.* **124**, 1285–1297 (2025).
18. H. N. Lekkerkerker, R. Tuinier, M. Vis, *Colloids and the Depletion Interaction* (Springer Nature, Cham, Switzerland, 2024), pp. 18–19.
19. M. Brust *et al*., The plasma protein fibrinogen stabilizes clusters of red blood cells in microcapillary flows. *Sci. Rep.* **4**, 4348 (2014).
20. D. Flormann *et al*., The buckling instability of aggregating red blood cells. *Sci. Rep.* **7**, 7928 (2017).
21. A. Rabe *et al*., The erythrocyte sedimentation rate and its relation to cell shape and rigidity of red blood cells from chorea-acanthocytosis patients in an off-label treatment with dasatinib. *Biomolecules* **11**, 727 (2021).
22. A. K. Dasanna *et al*., Erythrocyte sedimentation: Effect of aggregation energy on gel structure during collapse. *Phys. Rev. E* **105**, 024610 (2022).
23. F. Maurer *et al*., Continuous Percoll gradient centrifugation of erythrocytes–Explanation of cellular bands and compromised age separation. *Cells* **11**, 1296 (2022).
24. F. Charru, *Hydrodynamic Instabilities. Cambridge Texts in Applied Mathematics* (Cambridge University Press, 2011), vol. 37.
25. R. E. Ecke, Chaos, patterns, coherent structures, and turbulence: Reflections on nonlinear science. *Chaos* **25**, 097605 (2015).
26. A. De Wit, Chemo-hydrodynamic patterns and instabilities. *Annu. Rev. Fluid Mech.* **52**, 531–555 (2020).
27. M. Ben Amar, P. Ciarletta, P. A. Haas, Morphogenesis in space offers challenges and opportunities for soft matter and biophysics. *Commun. Phys.* **6**, 150 (2023).
28. M. C. Cross, P. C. Hohenberg, Pattern formation outside of equilibrium. *Rev. Mod. Phys.* **65**, 851 (1993).
29. S. A. Newman, W. D. Comper, 'Generic' physical mechanisms of morphogenesis and pattern formation. *Development* **110**, 1–18 (1990).
30. J. A. Davies, F. Glykofrydis, Engineering pattern formation and morphogenesis. *Biochem. Soc. Trans.* **48**, 1177–1185 (2020).
31. T. Y. C. Tsai *et al*., An adhesion code ensures robust pattern formation during tissue morphogenesis. *Science* **370**, 113–116 (2020).
32. Z. R. Sudderick, J. D. Glover, Periodic pattern formation during embryonic development. *Biochem. Soc. Trans.* **52**, 75–88 (2024).
33. S. Gao, L. Chang, M. Perc, Z. Wang, Turing patterns in simplicial complexes. *Phys. Rev. E* **107**, 014216 (2023).
34. A. M. Turing, The chemical basis of morphogenesis. *Bull. Math. Biol.* **52**, 153–197 (1990).
35. L. Katz, L. Silva-Dias, M. Dolnik, Turing patterns in the chlorine dioxide-iodine-malonic acid reaction-diffusion batch system. *J. Chem. Educ.* **101**, 1387–1393 (2024).
36. M. Bengfort, H. Malchow, F. M. Hilker, The Fokker–Planck law of diffusion and pattern formation in heterogeneous environments. *J. Math. Biol.* **73**, 683–704 (2016).
37. J. A. Carrillo, K. Craig, Y. Yao, *Aggregation-Diffusion Equations: Dynamics, Asymptotics, and Singular Limits*, N. Bellomo, P. Degond, E. Tadmor, Eds. (Springer International Publishing, Cham, Switzerland, 2019), pp. 65–108.
38. S. Fagioli, E. Radici, Solutions to aggregation-diffusion equations with nonlinear mobility constructed via a deterministic particle approximation. *Math. Model. Methods Appl. Sci.* **28**, 1801–1829 (2018).
39. M. Te Vrugt, J. Bickmann, R. Wittkowski, Effects of social distancing and isolation on epidemic spreading modeled via dynamical density functional theory. *Nat. Commun.* **11**, 5576 (2020).
40. A. Bogdanova, L. Kaestner, Early career scientists' guide to the red blood cell-don't panic! *Front. Physiol.* **11**, 588 (2020).
41. H. B. Weems, L. S. Lessin, Erythrocyte density distribution in sickle cell anemia. *Acta Haematol.* **71**, 361–370 (1984).
42. V. L. Lew, R. M. Bookchin, Ion transport pathology in the mechanism of sickle cell dehydration. *Physiol. Rev.* **85**, 179–200 (2005).
43. U. M. B. Marconi, P. Tarazona, Dynamic density functional theory of fluids. *J. Chem. Phys.* **110**, 8032–8044 (1999).
44. H. Löwen, *Applications of Density Functional Theory in Soft Condensed Matter* (World Scientific, 2010), pp. 9–45.
45. A. P. Philipse, B. W. M. Kuipers, Second virial coefficients of dipolar hard spheres. *J. Phys.: Condens. Matter* **22**, 325104 (2010).
46. A. Karmakar, G. W. Burgreen, G. Rydquist, J. F. Antaki, A homogenized two-phase computational framework for meso- and macroscale blood flow simulations. *Comput. Methods Programs Biomed.* **247**, 108090 (2024).
47. C. P. Royall, J. Dzubiella, M. Schmidt, A. Van Blaaderen, Nonequilibrium sedimentation of colloids on the particle scale. *Phys. Rev. Lett.* **98**, 188304 (2007).
48. J. Dzubiella, C. N. Likos, Mean-field dynamical density functional theory. *J. Phys.: Condens. Matter* **15**, L147–L154 (2003).
49. H. Lei, G. E. Karniadakis, Quantifying the rheological and hemodynamic characteristics of sickle cell anemia. *Biophys. J.* **102**, 185–194 (2012).
50. N. Moreno *et al*., Aggregation and disaggregation of red blood cells: Depletion versus bridging. *Biophys. J.* **124**, 1285–1297 (2025).
51. F. M. Maurer, Nvidia CUDA compiler implementation of red blood cell pattern formation in a density gradient during sedimentation (2025). https://github.com/FelixMaurer/RedPatterns. Accessed 3 October 2025.
52. M. Diez-Silva, M. Dao, J. Han, H. T. Lim, S. Suresh, Shape and biomechanical characteristics of human red blood cells in health and disease. *MRS Bull.* **35**, 382–388 (2010).
53. T. John *et al*., Viscosity and density measurements on the cytosol of human red blood cells. *Biophys. J.* **124**, 2668–2676 (2025).
54. F. Maurer et al., Data for "Band pattern formation of erythrocytes in density gradients isdue to competing aggregation and net buoyancy." Figshare. https://doi.org/10.6084/m9.figshare.29098733.v1. Accessed 3 October 2025.
55. C. S. Plüisch, R. Stuckert, A. Wittemann, Direct measurement of sedimentation coefficient distributions in multimodal nanoparticle mixtures. *Nanomaterials* **11**, 1027 (2021).